Size-dependent characterization of embedded Ge nanocrystals: Structural and thermal properties

L. L. Araujo,* R. Giulian, D. J. Sprouster, C. S. Schnohr, D. J. Llewellyn, and P. Kluth
Department of Electronic Materials Engineering, Research School of Physical Sciences and Engineering, Australian National University, Canberra, Australian Capital Territory 0200, Australia

D. J. Cookson
Australian Synchrotron Research Program, Building 434, 9700 South Cass Avenue, Argonne, Illinois 60439, USA

G. J. Foran
Australian Nuclear Science and Technology Organisation, Menai, New South Wales 2234, Australia

M. C. Ridgway
Department of Electronic Materials Engineering, Research School of Physical Sciences and Engineering, Australian National University, Canberra, Australian Capital Territory 0200, Australia
(Received 11 December 2007; revised manuscript received 28 July 2008; published 25 September 2008)

A combination of conventional and synchrotron-based techniques has been used to characterize the size-dependent structural and thermal properties of Ge nanocrystals (NCs) embedded in a silica (a-SiO_2) matrix. Ge NC size distributions with four different diameters ranging from 4.0 to 9.0 nm were produced by ion implantation and thermal annealing as characterized with small-angle x-ray scattering and transmission electron microscopy. The NCs were well represented by the superposition of bulklike crystalline and amorphous environments, suggesting the formation of an amorphous layer separating the crystalline NC core and the a-SiO_2 matrix. The amorphous fraction was quantified with x-ray-absorption near-edge spectroscopy and increased as the NC diameter decreased, consistent with the increase in surface-to-volume ratio. The structural parameters of the first three nearest-neighbor shells were determined with extended x-ray-absorption fine-structure (EXAFS) spectroscopy and evolved linearly with inverse NC diameter. Specifically, increases in total disorder, interatomic distance, and the asymmetry in the distribution of distances were observed as the NC size decreased, demonstrating that finite-size effects govern the structural properties of embedded Ge NCs. Temperature-dependent EXAFS measurements in the range of 15–300 K were employed to probe the mean vibrational frequency and the variation of the interatomic distance distribution (mean value, variance, and asymmetry) with temperature for all NC distributions. A clear trend of increased stiffness (higher vibrational frequency) and decreased thermal expansion with decreasing NC size was evident, confirming the close relationship between the variation of structural and thermal/vibrational properties with size for embedded Ge NCs. The increase in surface-to-volume ratio and the presence of an amorphous Ge layer separating the matrix and crystalline NC core are identified as the main factors responsible for the observed behavior, with the surrounding a-SiO_2 matrix also contributing to a lesser extent. Such results are compared to previous reports and discussed in terms of the influence of the surface-to-volume ratio in objects of nanometer dimensions.

DOI: 10.1103/PhysRevB.78.094112 PACS number(s): 61.46.−w, 81.07.−b, 61.05.cj, 85.40.Ry

I. INTRODUCTION

Intensive research has been directed toward nanomaterials and related phenomena in recent years due to the intriguing new properties observed at this scale and the corresponding potential for new technological applications. In particular, Ge nanocrystals (NCs) are of interest given their ability to emit light[1] (controversies on the origin of the phenomenon notwithstanding[2]) and store carriers.[3] As a consequence, Ge NCs are promising candidates for novel optoelectronic and nonvolatile memory device applications.

The growth and/or characterization of Ge NCs have been extensively reported.[1–23] The two main routes to producing NCs are chemical methods (see Ref. 4, for example), usually yielding freestanding or solution-dispersed NCs, and physical methods (see Refs. 1 and 5–8, for example), typically yielding NCs embedded in (or deposited on) a solid matrix. The properties of embedded NCs are expected to be governed by their size given the absence of chemical interaction with ligands or surfactants.[24] Furthermore, superior mechanical, thermal, and/or chemical stability is generally achieved with NCs embedded in a matrix. Among the physical methods, ion implantation is a versatile and well-established means of producing both metallic and semiconductor NCs.[25,26] Thermally grown silica (a-SiO_2) is usually the matrix of choice given the advantages of stability, a relatively inert nature, and compatibility with Si-based electronics.

The electronic and vibrational densities of states of a small cluster are very sensitive to the number of atoms contained therein. Thus size is expected to have profound impact not only on the structural properties of Ge NCs but also on the melting temperature,[27] heat capacity,[28] and superconducting transition temperature,[26] all of which depend on the vibrational dynamics of the NCs. Size effects can depend on: (i) the number of surface atoms relative to the total number of atoms (or equivalently the surface-to-volume ratio), expected to scale with D^{-1} or $N^{-1/3}$, where D and N are the

diameter and total number of atoms, respectively; or (ii) quantum phenomena (which scale with D^{-2}) originating from the discreteness of electronic states and band-gap variation with NC size.[29,30] The need for systematic size-dependent studies is thus paramount in identifying and quantifying the evolution of the properties of NCs as a function of their dimensions.

For this report we study the size-dependent structural and thermal properties of Ge NCs grown in an a-SiO_2 matrix by ion implantation and thermal annealing. A combination of conventional techniques [Rutherford backscattering spectrometry (RBS), transmission electron microscopy (TEM), and Raman spectroscopy] and synchrotron-based methods [x-ray-absorption near-edge structure (XANES), extended x-ray-absorption fine-structure (EXAFS), and small-angle x-ray scattering (SAXS) spectroscopies] has been utilized for characterization purposes. RBS was used to measure the depth distribution of Ge atoms, while TEM and SAXS yielded the NC size distribution. XANES measurements allowed quantification of the amorphous and crystalline fractions in the Ge NCs, while Raman spectroscopy was applied to qualitatively support the TEM, SAXS, and XANES results. Finally, the structural parameters for the first three nearest-neighbor (NN) shells surrounding a Ge absorber were determined with EXAFS. By combining results from these complementary techniques, we achieved a detailed picture of the size-dependent structural properties of Ge NCs. Our study indicates that Ge NCs embedded in a-SiO_2 retained a bulklike crystalline core with a thin amorphouslike Ge layer separating the core and amorphous silica matrix. The structural parameters of the first three NN shells scaled linearly with the inverse NC diameter, demonstrating that finite-size effects govern the structural properties of these embedded Ge NCs.

By performing temperature-dependent EXAFS measurements, it is possible to obtain accurate information on the variation of the mean value (interatomic distance), variance (Debye-Waller factor), and asymmetry (third cumulant) of the first-shell interatomic distance distribution in the measured temperature range. The thermal expansion, thermal and structural contributions to total disorder (and mean vibrational frequency) and anharmonicity of the effective pair potential, respectively, can be extracted from the experimental data by adequate combination of a correlated Debye or Einstein model and thermodynamic perturbation theory.[31–34] Fornasini and co-workers[31,32] recently reviewed advances on the use of EXAFS in studying thermal/vibrational properties of crystalline materials and highlighted the differences between parameters measured by EXAFS and Bragg scattering [x-ray diffraction (XRD)]. We have previously shown that this well-established approach can be extended to the study of elemental metal and semiconductor NCs embedded in a-SiO_2.[35,36] Here we further advance the study for Ge NCs, evaluating the effect of Ge NC size on the thermal/vibrational properties. EXAFS measurements were also performed on bulk crystalline Ge (c-Ge) and amorphous Ge (a-Ge) to allow the crystalline-nanocrystalline-amorphous comparison.

Details of the experimental conditions are found in Sec. II. Section III presents the results and discussion, and conclusions are summarized in Sec. IV.

II. EXPERIMENTAL DETAILS

Ion implantations of 2.0 MeV $^{74}Ge^{+1}$ ions to a fluence of 1×10^{17} cm^{-2} were performed at liquid-nitrogen temperature into 2.0-μm-thick a-SiO_2 layers grown on Si (100) wafers by wet thermal oxidation. Samples were then annealed under forming gas (5% H_2 in N_2) with one of these four different temperature/time combinations: 1060 °C/1 h, 1100 °C/0.33 h, 1100 °C/1 h, or 1100 °C/10 h. Ge NC formation and growth resulted in all cases.

RBS measurements were performed with 3.5 MeV $^4He^{+2}$ ions and a Si surface-barrier detector positioned at a scattering angle of 168°. RBS spectra were analyzed with the RUMP program.[37]

Cross-sectional TEM images were acquired in bright-field mode using a Philips CM300 FEI microscope and 300 keV electrons. Samples were prepared with a standard ion-beam-milling protocol.

Transmission SAXS measurements were performed at beamline 15ID-D of the Advanced Photon Source, USA, using a camera length of 1870 mm and 11.3 keV x rays. Scattering images were recorded with a MAR-165 charge coupled device (CCD) detector at an exposure time of 5 s. Data were analyzed with the IRENA 2 package[38] based on a maximum entropy method.[39,40] SAXS samples were prepared so as to eliminate scattering from the substrate and enable quantitative comparison between samples with different NC concentrations. The Si substrate thickness was first reduced from 540 to 100 μm by mechanical grinding. A concavity was then formed at the back of the Si substrate with dimple grinding, yielding a residual thickness of 20 μm at the concavity center. The sample was then chemically etched in 12.5M KOH (selective to Si) until a 1 mm diameter hole was formed at the concavity center below the a-SiO_2 layer. A self-supporting, substrate-free SAXS sample of the NC-containing a-SiO_2 layer was thus obtained.

Raman spectroscopy was performed with a Dilor Super Labram spectrometer equipped with a liquid-nitrogen-cooled CCD detector. Samples were illuminated with the 514.5 nm line of an Ar^{+1} ion laser with an Olympus 2 μm objective used to focus the laser and collect scattered light. With our SAXS sample preparation method described above, the common Raman artifact[16,17] near ~300 cm^{-1} resulting from the overlap of the transverse-acoustic second-order peak for Si and the first-order optical peak for Ge was completely eliminated without the need to use special measurement geometries (crossed polarization)[16] or posterior subtraction of spectra.[15]

XANES/EXAFS measurements at the Ge K edge (11.103 keV) were performed at eight different temperatures in the range of 15–300 K at beamline 20-B of the Photon Factory, Japan. Measurement temperatures were stable to ±1 K. Fluorescence spectra were recorded with a 6×6 Ge pixel array detector. For energy calibration, a bulk crystalline Ge reference foil was measured simultaneously in transmission mode. The Si (111) monochromator was detuned by 50% for harmonic rejection. XANES/EXAFS samples were also prepared using a novel technique to yield an improved signal-to-noise ratio and enable high-resolution measurements up to 16 $Å^{-1}$. The Si substrate below the NC-containing a-SiO_2

layer was first removed through a combination of mechanical grinding and selective chemical etching. The freestanding NC-containing a-SiO_2 layers were then simply stacked together.[41] Bulk c-Ge and a-Ge standards appropriate for fluorescence measurements were prepared by molecular-beam epitaxy and ion implantation, as described in Ref. 5.

Fluorescence spectra were first averaged with the program AVERAGE.[42] Data processing and analysis were then performed using the ATHENA and ARTEMIS (Ref. 43) graphical user interfaces for the IFEFFIT (Ref. 44) and FEFF (Ref. 45) codes. The EXAFS oscillations were extracted from the spectra by background subtraction (removing the raw absorbance) via the AUTOBK algorithm implemented in ATHENA.[43] Data were then Fourier transformed using a Hanning window 0.8 $Å^{-1}$ in width and ranging from 4.1–15.1 $Å^{-1}$ in photoelectron wave-number (k) space. Back transforming from radial distance (R) space, the window defining the fitting region was again of the Hanning type and of 0.2 Å width and ranged from 1.5–4.8 Å for the structural study using the 15 K data and 1.5–2.7 Å for the temperature-dependent analysis. Values of the energy shift parameter ΔE_0 were refined using ARTEMIS and following the procedure suggested in Ref. 46 to align the k scale of the theoretical standard for all samples as well as avoid distortions in the structural parameters due to a poor choice of edge energy position E_0. Effective scattering amplitudes and phase shifts were calculated *ab initio* with FEFF8.[45]

Spectra were fitted in ARTEMIS (Ref. 43) using two different procedures for the low-temperature structural study and the temperature-dependent study. For the former, a full multiple-scattering approach with three single-scattering and four multiple-scattering paths was applied to probe up to the third NN shell, as described elsewhere.[47] For the latter, only the first NN shell was analyzed (following the multiple-data set fitting approach described in Ref. 36) due to the smearing out of second and third NN contributions with increasing temperature for the Ge NC samples. Coordination numbers CN were fixed to bulk values for c-Ge and fitted for the a-Ge and Ge NC samples. These CN values determined from the low-temperature spectra were kept constant during the temperature-dependent analysis. Individual interatomic distances R, Debye-Waller factors σ^2, and third cumulants C_3 were determined for each NN shell, while the evolution with temperature of R, σ^2, and C_3 was determined for the first NN shell only. Each data set was fitted simultaneously with multiple k weightings of 1–4 to reduce correlations between the fitting parameters. The passive electron reduction factor S_0^2 and the energy shift parameter ΔE_0 were determined from c-Ge and kept constant for all other samples. The same ΔE_0 was assigned for all paths, assuming no charge distribution effects in elemental Ge.[48] The values obtained were $S_0^2 = 0.99 \pm 0.05$ and $\Delta E_0 = 0.3 \pm 1.1$ eV.

III. RESULTS AND DISCUSSION

A. Depth and size distributions

1. Depth distribution

The depth distribution of implanted Ge atoms in the a-SiO_2 layer was measured before and after annealing with RBS. The peak concentration was ~3 at. % centered at a depth of ~1.4 μm with a full width at half maximum (FWHM) of ~0.5 μm (±10%). As apparent from Fig. 1, no significant redistribution of Ge was observed, within the RBS detection limit, for all annealing conditions. The inset shows the Ge signal after subtracting the a-SiO_2 background and converting from energy to depth scale using the mean energy approximation.[49]

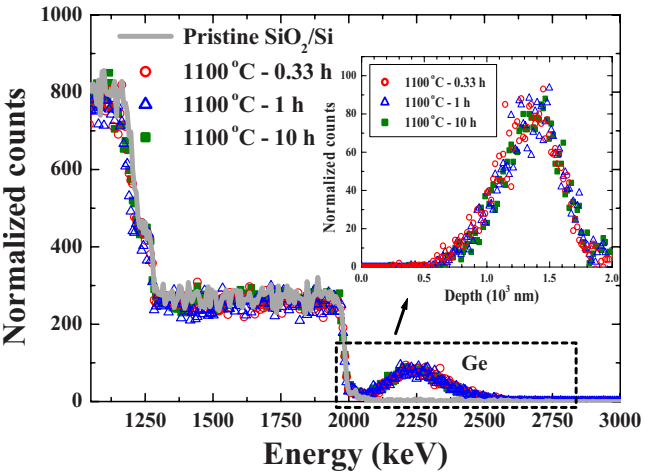

FIG. 1. (Color online) RBS spectra for a pristine SiO_2/Si sample (line) and three samples implanted with Ge and annealed under different conditions (symbols). The inset shows the Ge distribution as a function of SiO_2 depth.

The lack of thermally induced diffusion has been observed previously for various elemental NCs annealed under forming gas; for example, see Ref. 26. This nondiffusive, nonreactive behavior is consistent with the model of Heinig *et al.*[18] that correlates the redistribution of implanted atoms to the presence of H_2O and O_2 impurities. In our case, Ge diffusion,[13,21] GeO_x ($x \leq 2$) formation,[13,21] and NC passivation[50] are further inhibited by the significant spatial separation of the center of the Ge atomic distribution from both the surface (~1.4 μm) and the SiO_2/Si interface (~0.6 μm).

2. Size distribution

Ge NC size distributions were determined from SAXS measurements. Figure 2 shows the scattered intensity mea-

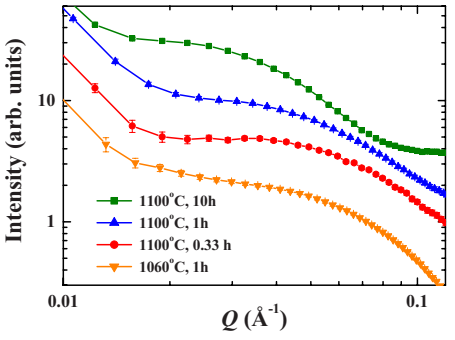

FIG. 2. (Color online) SAXS spectra for Ge NC samples after subtraction of the SiO_2 background, measured from an unimplanted sample (not shown). Spectra are offset for clarity.

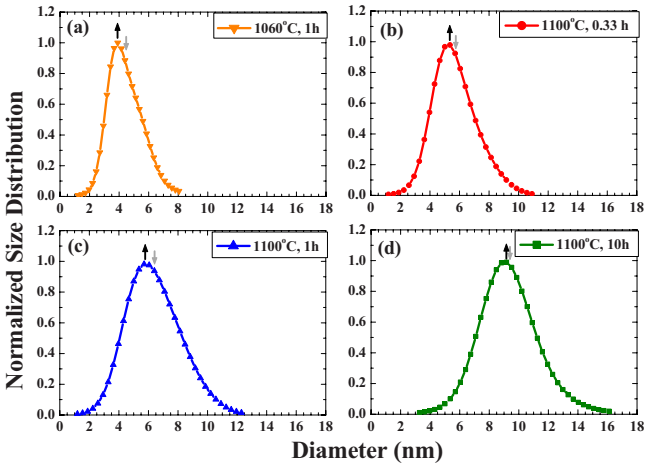

FIG. 3. (Color online) Size distributions of the Ge NCs grown under the specified annealing conditions (legends), as obtained from SAXS analysis. The up arrows indicate the position of the maximum value and the down arrows show the position of the mean value of the size distributions. Such values are listed in Table I.

sured for all samples after subtraction of the a-SiO_2 background. The scattering vector Q range for the analysis was 0.015–0.12 $Å^{-1}$ and a maximum entropy approach was applied to fit the curves.[39,40] The NC shape was assumed to be spherical, consistent with the TEM observations presented below. Figure 3 shows the size distributions obtained after fitting the data in Fig. 2, normalized to unity for comparison. They are asymmetric, being skewed toward larger diameters. This asymmetry decreases and the FWHM increases with an increase in annealing temperature and time. The value at the maximum and the statistical mean differ slightly, as indicated by the arrows in Fig. 3, as a result of the asymmetry. Henceforth, the value at the maximum will be used when discussing the size dependence of the structural and thermal properties. Values at the distribution maximum, the statistical mean, the FWHM, and the half-width at half maximum (HWHM) to each side of the maximum are listed in Table I.

Complementary TEM images from depths near the Ge atomic concentration maximum are shown in Fig. 4. They illustrate the spherical nature of the NCs and the increase in size with annealing temperature or time as first apparent from SAXS measurements. The size distributions determined by TEM and SAXS were consistent and no Ge NCs were observed close to either the SiO_2 surface or the SiO_2/Si interface.

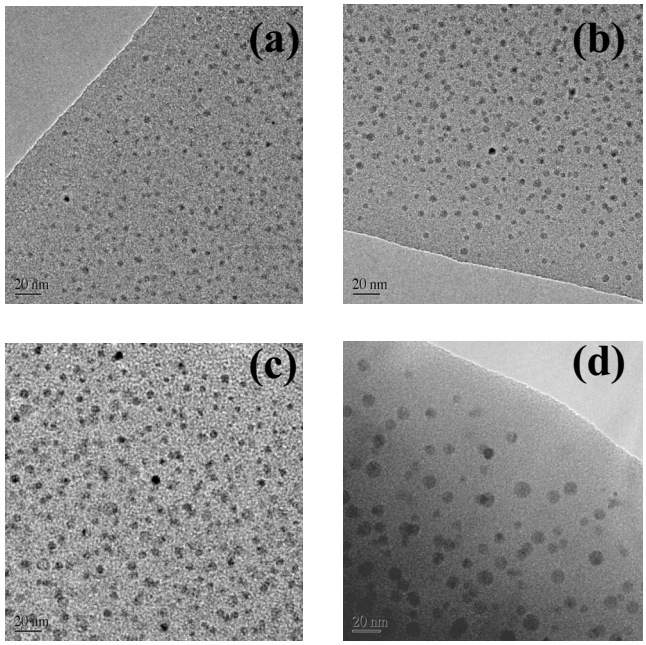

FIG. 4. TEM images recorded near the Ge concentration maximum for samples annealed at (a) 1060 °C, 1 h; (b) 1100 °C, 0.33 h; (c) 1100 °C, 1 h; and (d) 1100 °C, 10 h.

B. Structural properties and size dependence

1. XANES analysis

Based on the SAXS results presented previously, samples will now be identified as 4, 5, 6, or 9 nm Ge NCs (for the annealing conditions 1060 °C/1 h, 1100 °C/0.33 h, 1100 °C/1 h, and 1100 °C/10 h, respectively). XANES spectra for the Ge NC samples and bulk standards are shown in Fig. 5. The XANES region is considered to extend some tens of eV beyond the absorption edge,[51] where the excited photoelectron has enough kinetic energy to reach the continuum but its wavelength is larger than the interatomic distance between the absorbing atom and first NN. At such low kinetic energies, the photoelectron is strongly scattered by neighboring atoms and the wave function is governed by multiple scattering (MS) effects.[51] The latter may produce sharp features in the spectrum, as apparent in Fig. 6 for c-Ge and c-GeO_2, and can be used to fingerprint chemical bonding, electronic configuration, and site symmetry around the absorber. Comparing the spectra for bulk a-Ge and c-Ge, the

TABLE I. Values, in nanometers, of the mean, the maximum, the FWHM, and the HWHM for the Ge NC size distributions obtained from SAXS analysis. The errors are estimated as 5% of the listed values. The labels "Low" and "High" in columns 5 and 6 are relative to the lower-size side and higher-size side of the maximum value listed in column 3, respectively. Errors of 5% for the crystalline fractions are estimated based on results obtained when the fitting range is varied by 20%.

Annealing conditions	Mean	Maximum	FWHM	Low HWHM	High HWHM	Crystalline fraction
1060 °C, 1 h	4.5	3.9	2.5	1.0	1.5	0.512
1100 °C, 0.33 h	5.7	5.3	3.1	1.4	1.7	0.523
1100 °C, 1 h	6.4	5.9	4.2	1.9	2.3	0.615
1100 °C, 10 h	9.4	9.1	4.2	2.0	2.2	0.759

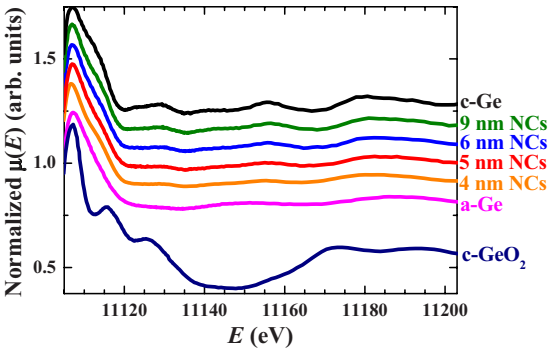

FIG. 5. (Color online) XANES region of the K-edge absorption spectrum for bulk c-Ge, a-Ge, and c-GeO_2, as well as for the four different Ge NC samples. Spectra have been vertically shifted for clarity.

former is rather featureless, while the latter shows characteristic peaks. Similar observations have been reported for Si where oscillations due to MS were observed for c-Si within ~70 eV of the K edge, while no oscillations were apparent for a-Si.[52] Most of the MS contributions stemmed from double-scattering paths involving atoms from the first and second NN shells.[52]

In the XANES spectra of the Ge NC samples, no indication of Ge-O bonds is apparent for any sample, in contrast to several previous reports.[11,21] We therefore exclude the presence of a significant fraction of isolated Ge atoms dissolved in the silica matrix. Bulklike c-Ge features are observed in the spectra of all NC samples. Such features grow weaker as the NC size decreases while simultaneously the similarity between the Ge NC and bulk a-Ge spectra increases. Clearly, the Ge NC spectrum appears as a combination of the c-Ge and a-Ge spectra. The Ge NC spectra were thus fitted as a linear combination of the two bulk standards. The fitting was performed with ATHENA (Ref. 43) over an energy range of −30 to 100 eV above the absorption edge. Figure 6 demonstrates that the XANES spectra of Ge NCs are accurately reproduced as a combination of bulklike amorphous and crystalline environments. The arrows in Fig. 6(a) indicate the MS features in the c-Ge spectrum that are also present for the Ge NCs.

Table I lists the fraction of Ge atoms in a bulklike crystalline environment as a function of NC size. Clearly the crystalline fraction decreases as the NCs become smaller or, equivalently, the surface-to-volume ratio increases. We suggest such results are consistent with the presence of an amorphous Ge layer separating the crystalline Ge core and the amorphous silica matrix, in good agreement with first-principles and empirical molecular-dynamics calculations for 1.0–2.5 nm freestanding Ge clusters[30,53] and 1.3–3.6 nm Si nanoparticles embedded in a-SiO_2.[54] Similar qualitative findings were also reported in a XANES study of 2.0–3.4 nm Si NCs embedded in a-SiO_2.[55] Using the NC diameter determined from SAXS measurements and the amorphous fraction determined from XANES measurements, we calculated an amorphous layer thickness of ~0.44 nm, independent of NC size. This provides further support for the presence of an amorphous layer separating a crystalline core and amorphous matrix. (We note a crystalline core is readily apparent in high-resolution TEM images, as previously presented.[36,56]) Our results also agree with photoemission spectroscopy measurements for freestanding Ge NCs of diameter ~7.0 nm and below, as produced by gas evaporation,[12,23] although we

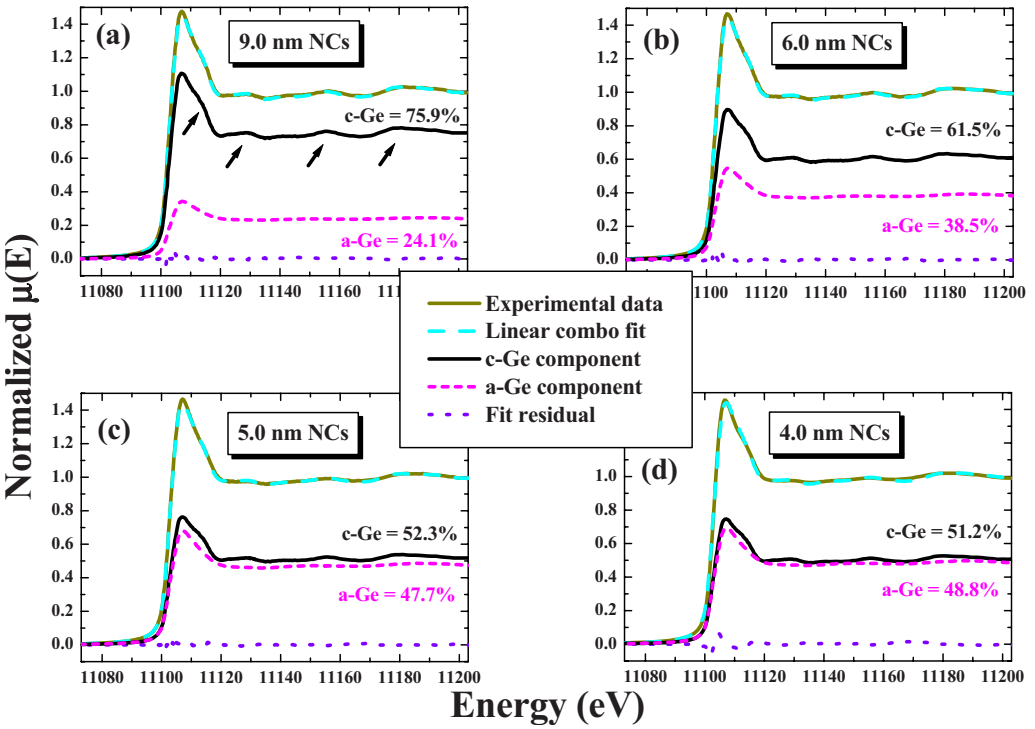

FIG. 6. (Color online) Linear combination fits to XANES spectra of Ge NCs using bulk c-Ge and a-Ge standards. The arrows in (a) indicate features that are characteristic of bulk c-Ge and are absent in the a-Ge spectrum.

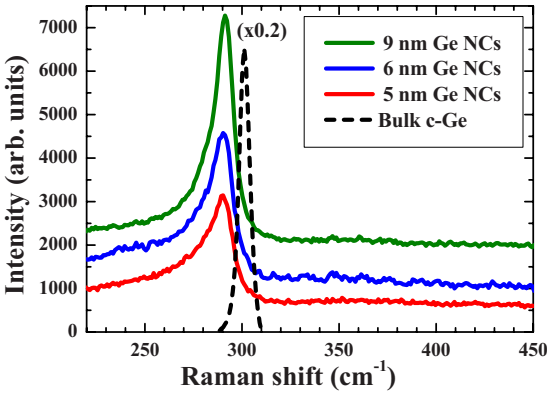

FIG. 7. (Color online) Raman spectra for bulk *c*-Ge and Ge NC samples. The bulk spectrum has been divided by 5 and the spectra have been offset for clarity.

point out that the growth/reconstruction dynamics might be different in both cases. Comparing bulk and NC samples, the authors showed that NCs were mainly bulklike crystalline but with distinct features indicative of structural disorder in the surface and near-surface regions. A distribution of bond angles and bond lengths, very similar to that observed for bulk *a*-Ge, was measurable in the NC surface region.[12] Frenkel *et al.*[57] combined EXAFS and diffraction anomalous fine-structure (DAFS) measurements to characterize samples containing both bulk *a*-Ge and nanocrystalline Ge. A similar approach could yield further evidence of the amorphouslike layer in our Ge NC samples.

2. Raman measurements

Raman spectra for Ge NCs and a bulk *c*-Ge standard are presented in Fig. 7. (As noted earlier, our sample preparation method eliminates interference from the second-order Raman peak for Si.) As anticipated, an increase in intensity and decrease in FHWM of the crystalline Ge-Ge scattering peak is readily apparent as the NCs increase in size. The low-frequency asymmetric broadening and redshift in the Raman spectra[58,59] due to finite-size effects are also observed. Some of the redshift also stems from an isotopic effect,[60] when comparing NCs comprised solely of ^{74}Ge and natural bulk *c*-Ge (~72.6 amu). The increase in peak area as the NCs increase in size is in very good quantitative agreement with the increase in crystalline fraction determined from the XANES analysis, thus reinforcing our results.

A scattering contribution from an *a*-Ge component, expected at ~260 cm^{-1}, could not be resolved as consistent with previous reports[14,15] where the authors suggested that the presence of the *a*-SiO_2 matrix stabilizes the surface atoms and reduces their contribution to the Raman intensity. Alternatively, the phonon density of states (DOS) may be large in the SiO_2 near ~260 cm^{-1}, enhancing the decay rate of surface-atom vibrations.[15]

3. EXAFS analysis

The structural parameters for the first three NN shells, including the coordination numbers and mean value, the Debye-Waller factor, and asymmetry (third cumulant) of the interatomic distance distribution were determined from EXAFS analysis. A cumulant expansion approach[61] was employed to account for possible asymmetric (third cumulant) and symmetric (fourth cumulant) deviations from a Gaussian distribution. Such deviations can result from the presence of thermal and/or structural disorder. Asymmetry can be non-negligible for bulk crystalline materials even at low temperatures[62] and must not be ignored at high temperatures.[32,36,63–65] It is also significant for bulk amorphous materials[64,65] and NCs (Refs. 36, 66, and 67) at low temperatures. Failure to account for asymmetry yields erroneous structural parameter values, particularly for the interatomic distance. For this report, both the third and fourth cumulants were included in the fitting procedure. While the latter proved to be negligible, the former was significant.

Figures 8(a) and 8(b) show isolated k^3-weighted EXAFS spectra for the bulk standards and NC samples, respectively. Bulklike crystalline features are present in all NC spectra. Like for the XANES spectra, these features grow weaker as the NCs become smaller and the spectra more closely resemble that of bulk *a*-Ge. Figures 8(c) and 8(d) show the resulting Fourier transforms (FTs) for the bulk and NC samples, respectively. Scattering contributions from the first three NN shells [indicated in Fig. 8(d)] are evident for the *c*-Ge and Ge NC samples, while only the first NN shell is apparent for *a*-Ge. The structural disorder inherent with the amorphous phase clearly precludes any contribution from higher shells.

4. Structural parameters and crystalline fraction

Figures 9(a)–9(d) show the first shell coordination numbers, interatomic distances, Debye-Waller factors, and third cumulants, respectively, as functions of the crystalline fraction determined with XANES. Figure 9(a) demonstrates that the coordination numbers for bulk *c*-Ge and *a*-Ge are comparable, consistent with previous reports. This phenomenon originates from the presence of three-, four-, and fivefold coordinated atoms in bulk *a*-Ge.[53,68,69] While the 9 nm NCs have a coordination number similar to that of the bulk, this parameter decreases as the NCs become smaller. This is a clear manifestation of finite-size effects where the increase in surface-to-volume ratio yields a relative increase in undercoordinated surface atoms. Such an effect is independent of the crystallographic phase (amorphous or crystalline) at the NC surface or interface with the matrix.

For the mean interatomic distance [Fig. 9(b)], the value for bulk *a*-Ge exceeds that of bulk *c*-Ge, again consistent with previous measurements[69,70] and explained by the same reasoning noted above for the coordination numbers. The 9 nm NCs exhibit an interatomic distance similar to that for bulk *c*-Ge. However, as the NC size decreases, the interatomic distance increases and approaches that for bulk *a*-Ge. This contradicts observations for metallic NCs,[66,71,72] where a decrease in size is accompanied by a contraction of the mean interatomic distance due to capillary pressure. For the present case, the increase in interatomic distance apparent in semiconductor NCs results from the increase in amorphous fraction with decreasing NC size. Metallic NCs do not

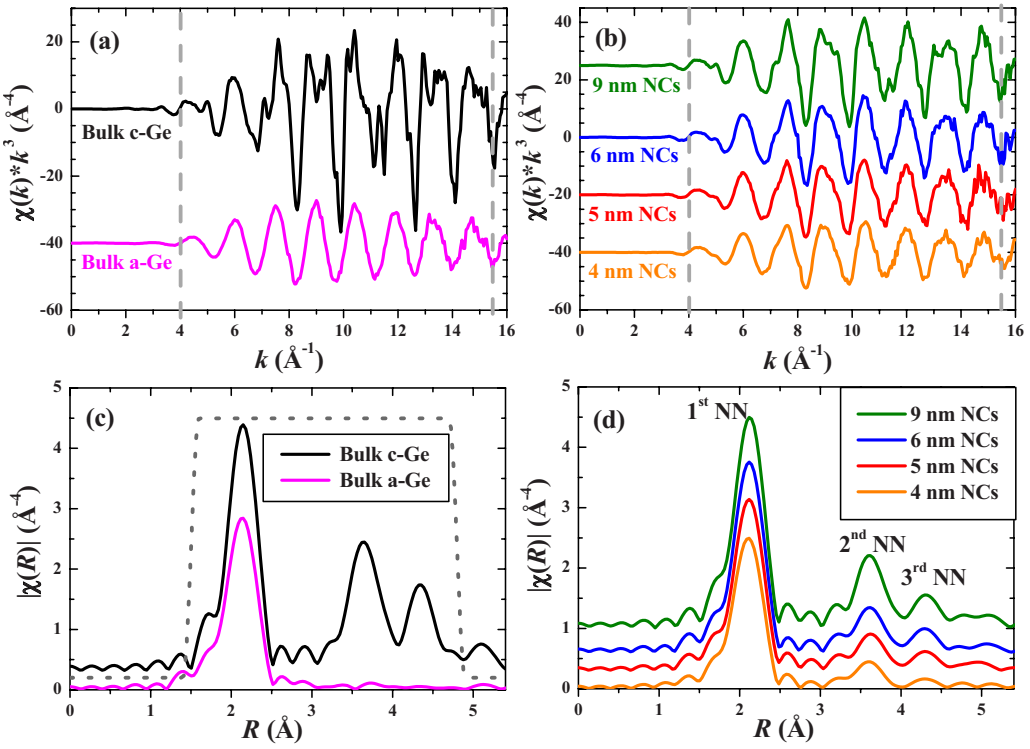

FIG. 8. (Color online) Top: Raw EXAFS oscillations obtained after background removal, multiplied by k^3, for (a) bulk *c*-Ge and *a*-Ge and (b) Ge NC samples. The vertical dashed lines indicate the data range used for the Fourier transforms. Bottom: Fourier-transformed EXAFS signal for (c) bulk *c*-Ge and *a*-Ge and (d) Ge NC samples. The dotted line in (c) indicates the window used for the full MS fits and the first three NN shells are labeled in (d). Spectra have been offset for clarity.

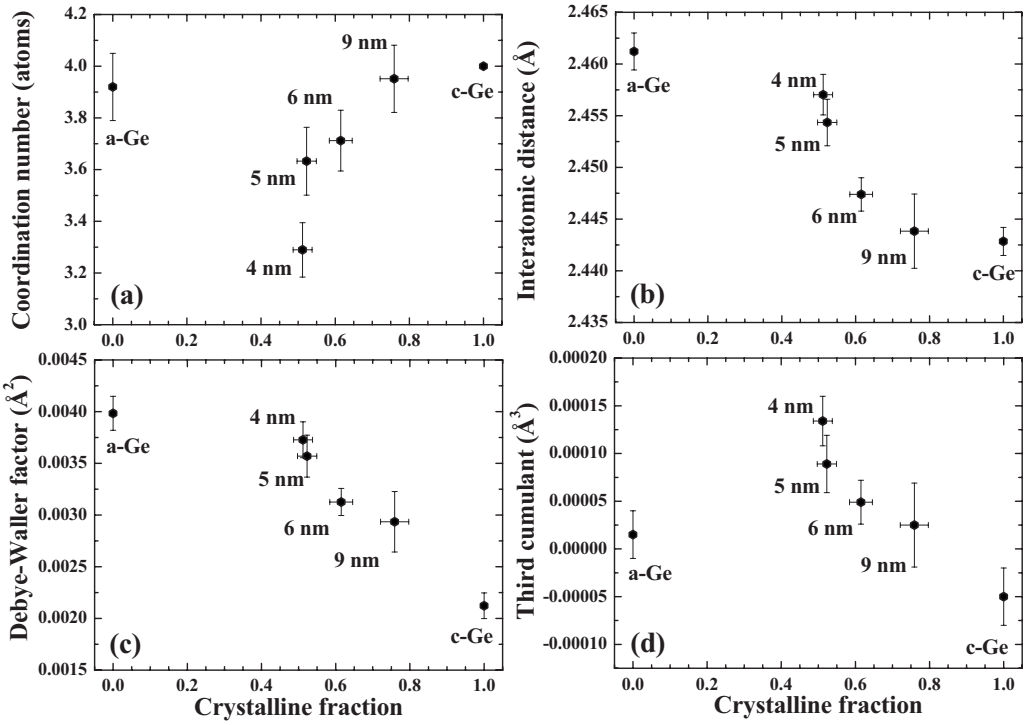

FIG. 9. Results obtained from EXAFS analysis for first NN shell (a) coordination numbers, (b) interatomic distances, (c) Debye-Waller factors, and (d) third cumulants, plotted as a function of the crystalline fraction determined with XANES.

exhibit a comparable amorphous component (unless subjected to ion irradiation subsequent to formation[73,74]).

Previous works reported the formation of embedded Ge NCs with the ST-12 phase rather than the diamond phase for small sizes (diameters <4 nm).[7,75] The bulk ST-12 phase shows a first NN shell interatomic distance 0.04 Å higher than the cubic diamond phase.[70] In principle, a cubic–to–ST-12 phase transformation would also yield a progressive interatomic distance increase with the decrease in NC size. We exclude this effect in our study because the interatomic distance increase observed here is less than half of the 0.04 Å reported in Ref. 70 and much closer to the increase observed for *a*-Ge relative to *c*-Ge.[69,70] Furthermore, XANES results indicate the presence of an amorphous contribution which accounts well for the observed increase in interatomic distances.

Results for the Debye-Waller factor [Fig. 9(c)] show the expected increase in structural disorder of bulk amorphous material relative to the crystalline phase as reported previously.[53,68,69,76] The 9 nm NCs exhibit a Debye-Waller factor value greater than that of bulk *c*-Ge due to the increased surface-to-volume ratio and the presence of an amorphous component. As the NC size decreases, this parameter increases such that the Debye-Waller factor for the 4 nm NCs is comparable to that of bulk *a*-Ge. Even smaller NCs should yield a Debye-Waller factor equal to that of bulk *a*-Ge [and consistent with amorphized Ge NCs (Refs. 5 and 77)] as the crystalline fraction becomes negligible.

A small nonzero third cumulant was measurable in the interatomic distance distributions for the first NN shell of the bulk standards, as previously reported.[62,69] For bulk *a*-Ge, the value of this parameter is dependent on the fabrication process (sputtering, evaporation, irradiation), the H content, and the extent of postamorphization structural relaxation.[69,78] For Ge NCs, asymmetry in the interatomic distance distribution increases as the NC size decreases and exceeds the value measured for *a*-Ge. We suggest that the increased surface-to-volume ratio for the NCs yields such an effect.

5. Size dependence of structural parameters for Ge NCs

In this section we describe the trends observed for the structural properties of the first three NN shells of Ge NCs as a function of size. Results are plotted as a function of inverse NC diameter in Fig. 10. Each column shows data for a given NN shell, while each row reports the results for one specific structural parameter. The first NN shell structural parameters discussed in Sec. III B 4 clearly scale as a linear function of inverse diameter (left column of Fig. 10). This indicates that finite-size effects, specifically the surface-to-volume ratio, govern the structural properties of embedded Ge NCs in addition to the crystalline and amorphous fractions discussed previously.

Though the uncertainty in the structural parameter determinations necessarily increases for shells beyond the first NN, trends comparable to those discussed above are still readily apparent and again demonstrate the significant influence of finite-size effects. Such influence is well demonstrated in the top row of Fig. 10 (coordination numbers). Full lines represent the size-dependent evolution of the coordination number calculated with a geometrical model[56] that assumes spherical Ge NCs with the diamond structure. The disagreement between the geometrical model and the experimental data increases dramatically for the higher shells, which are most sensitive to finite-size effects. Note that for the first shell all Ge atoms contribute to the EXAFS signal, whether in a crystalline or an amorphous environment. On the other hand, the latter do not yield a second- or third-shell scattering contribution. To account for the presence of an amorphous interfacial layer, the geometric model results were multiplied by the crystalline fraction as determined with XANES. As apparent in the top row graphs in Fig. 10, much better agreement with the experimental data is then achieved, further supporting our assertion that an amorphous layer separates the *a*-SiO_2 matrix and the *c*-Ge core in embedded Ge NCs.

C. Thermal properties and size dependence

Temperature-dependent EXAFS measurements in the range of 15–300 K were employed to probe the thermal expansion of interatomic distances and the mean vibrational frequency for all NC distributions. Figure 11 shows the background subtracted, k^1-weighted EXAFS oscillations and the corresponding non-phase-corrected FTs as a function of temperature for the biggest and smallest Ge NCs and bulk *a*-Ge. The high quality of the data is apparent from the EXAFS spectra presented in Figs. 11(a), 11(c), and 11(e). Although a second NN peak is visible at ~3.6 Å in the FT of the Ge NC samples at low temperatures [Figs. 11(b) and 11(d)], an increase in temperature (and therefore of thermal disorder) significantly reduces the amplitude. The even higher structural disorder of the amorphous phase precludes any higher NN contributions regardless of the temperature, as evident in Fig. 11(f).

1. Debye-Waller factors and Einstein temperatures

The experimental σ^2 values from EXAFS, which can be regarded as a measure of the total disorder or the variance of the interatomic distance distribution, are plotted as a function of measurement temperature in Fig. 12. The corresponding best fits with the Einstein model[36] are also included. The separate thermal and structural contributions to the total disorder,[79] expressed in terms of the Einstein temperature and static contribution to σ^2, respectively, are listed in Table II. As expected, σ^2 increases with temperature, reflecting the increase in amplitude of atomic movement around the equilibrium positions and the resulting increase in the variance of the interatomic distance distribution. σ^2 increases with temperature more rapidly for *a*-Ge compared to *c*-Ge, yielding a lower Einstein temperature indicative of lower bond strength or looser bonding. In contrast, for Ge NCs σ^2 increases with temperature more slowly than for *c*-Ge, resulting in higher Einstein temperatures consistent with stiffer bonding (in agreement with our previous report for a different Ge NC distribution[36]). A clear trend with Ge NC size is apparent and will be further discussed below.

One last point should be addressed regarding our obtained σ^2 values. It is well known that isotopic composition can

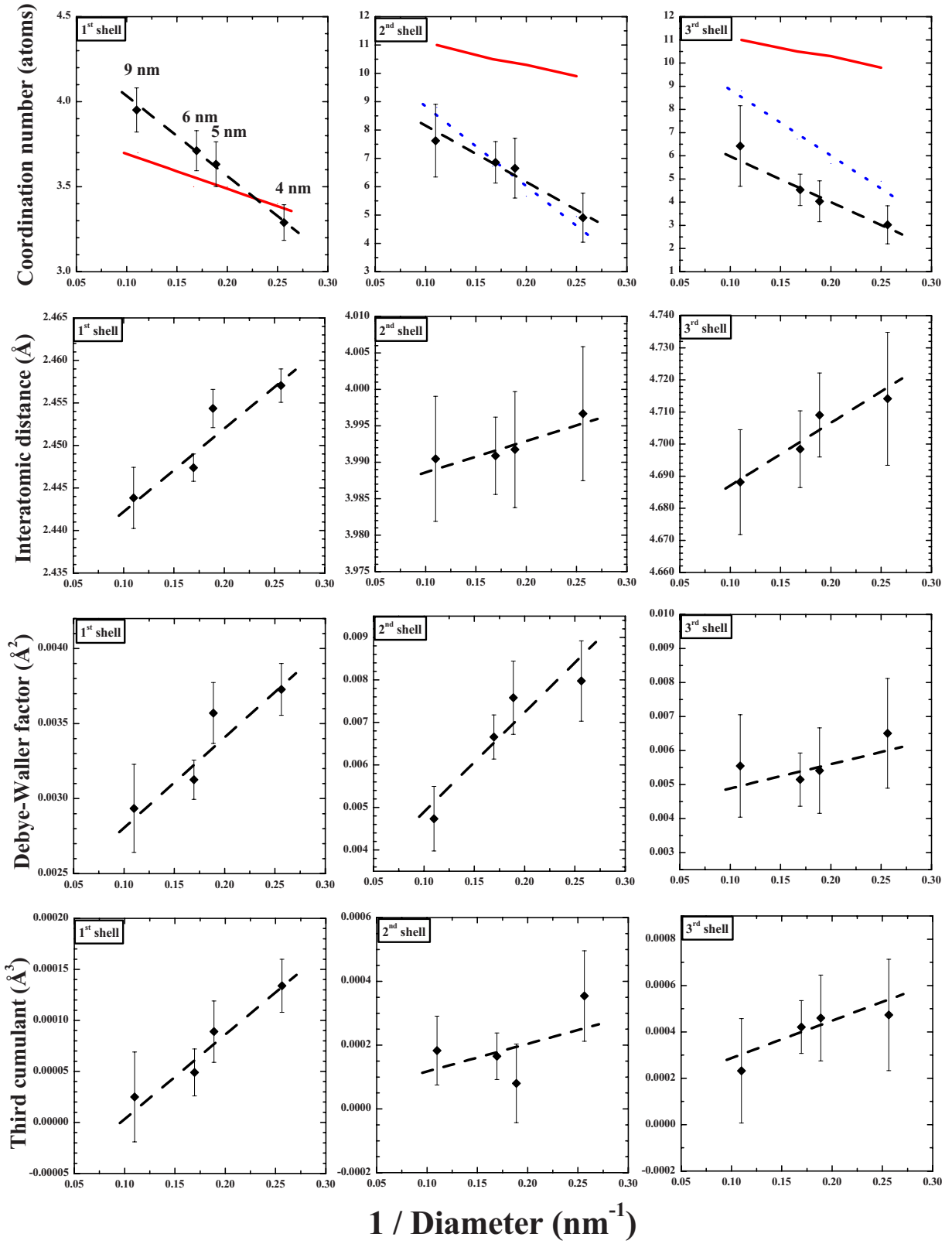

FIG. 10. (Color online) Size-dependent trends observed for the structural properties of the first three NN shells about a Ge absorber plotted as a function of inverse NC diameter. Symbols are experimental results and dashed lines are linear fits. Each column corresponds to a given NN shell, while each row relates to one structural parameter. The full lines are coordination numbers calculated according to a geometrical model, while the dash-dotted lines are the same coordination numbers multiplied by the crystalline fraction determined from XANES measurements.

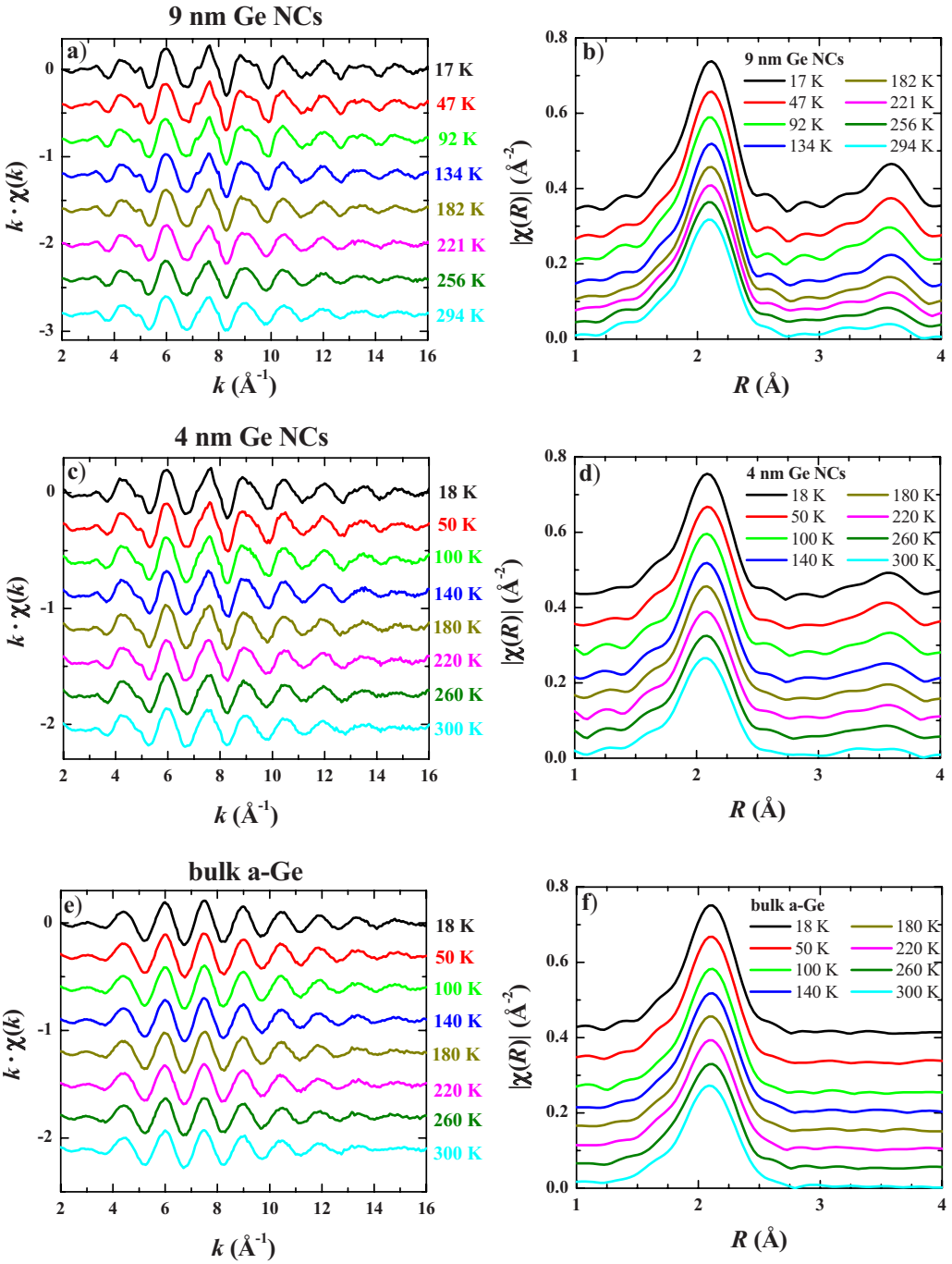

FIG. 11. (Color online) [(a), (c), and (e)] Raw EXAFS oscillations after background removal and [(b), (d), and (f)] corresponding Fourier transforms for the temperature-dependent measurements on the 9 nm Ge NCs [(a) and (b)], 4 nm Ge NCs [(c) and (d)], and bulk *a*-Ge [(e) and (f)] samples. Spectra are vertically offset for clarity.

affect the equilibrium crystal volume and the vibrational properties due to differences in zero-point motion of the nuclear masses.[60,80–83] A recent EXAFS study on bulk isotopically enriched ^{70}Ge and ^{76}Ge crystals reported a difference of 0.000 07 Å^2 in the σ^2 at 20 K, with the σ^2 for ^{76}Ge smaller due to its higher mass and thus reduced mean vibrational frequency.[80] Interestingly enough, such a small difference in σ^2 lead to a substantial difference of ~15 K between the Einstein temperatures for bulk crystalline ^{70}Ge and ^{76}Ge.

Since our NCs are produced by implanting ^{74}Ge but are compared to natural bulk Ge standards (^{Nat}Ge, ~72.6 amu), in principle it would be necessary to account for this isotopic effect before commenting on the differences between bulk and NCs. Nevertheless, we note that the mass difference in our case is four times smaller than that in Ref. 80. Thus the expected isotopic effect on the low-temperature σ^2 can be estimated as ~0.000 02 Å^2, well within the error bars even for the most optimistic studies. Furthermore, it becomes evi-

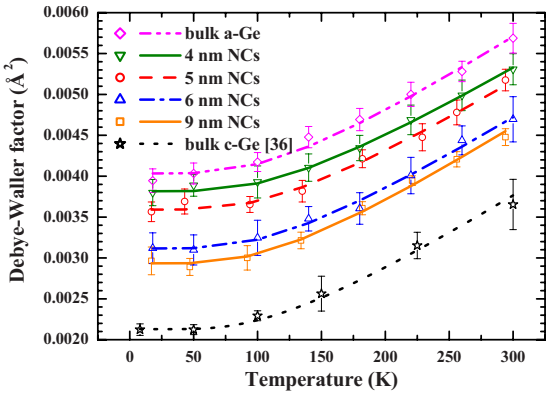

FIG. 12. (Color online) Debye-Waller factor values (symbols) and corresponding Einstein model fits (lines) obtained for the Ge NC and bulk *a*-Ge samples plotted as a function of measurement temperature. Data for *c*-Ge from Ref. 36 are also plotted for comparison. Corresponding fit results are listed in Table II.

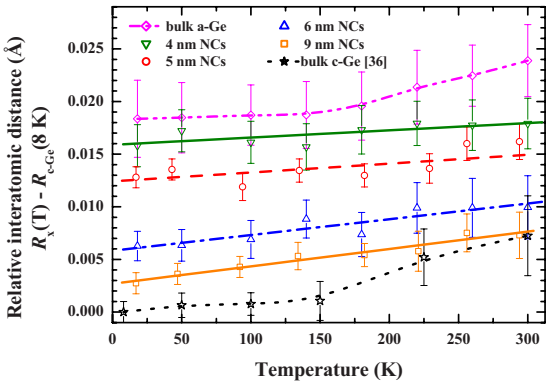

FIG. 13. (Color online) Evolution of the first NN shell mean interatomic distance as a function of measurement temperature. Experimental results (symbols) are given as values relative to the low-temperature distance obtained for *c*-Ge in order to highlight the structural and thermal differences between bulk and NCs. The lines have no physical meaning and simply highlight the temperature trend of the data. Data for *c*-Ge from Ref. 36 are also plotted for comparison.

dent that the differences between σ^2 for the bulk crystal and NCs are due to structural differences, amounting to $\sim 0.80 \times 10^{-3}$ Å^2, rather than due the subtle mass effect in zero-point motion mentioned in Ref. 80, which would be at least 40 times weaker in our case. Also, there is a clear trend for the increase in the low-temperature σ^2 with the decrease in NC size as shown in Figs. 10 and 12, even though all NCs were produced by implanting ^{74}Ge and have the same isotopic composition. This demonstrates that the isotopic effect has no significant influence on our size-dependent study or the bulk vs NC comparison presented here.

2. *Interatomic distances and thermal expansion*

The evolution of the interatomic distances with temperature for bulk *a*-Ge and Ge NCs is presented in Fig. 13. Values are relative to the low-temperature interatomic distance obtained for *c*-Ge (shown in Fig. 9) to highlight the structural and thermal differences between bulk and NCs. Table II lists the resulting linear thermal expansion ΔR and linear thermal expansion coefficient α_{EXAFS} in the range of 15–300 K, respectively defined as

$$\Delta R = R_{(300\ \mathrm{K})} - R_{(17\ \mathrm{K})}, \tag{1}$$

$$\alpha_{\mathrm{EXAFS}} = \frac{1}{R_0}\frac{\Delta R}{\Delta T}, \tag{2}$$

where R_0 is the low-temperature value obtained for *c*-Ge (2.443 Å).

A clear distinction should be made between the linear thermal expansion coefficients determined from EXAFS (α_{EXAFS}) and those determined from other techniques (α_L) such as XRD, which measure the variation in the mean distance between the equilibrium positions in the lattice. EXAFS measures the mean of instantaneous interatomic distances and is sensitive to correlation effects, yielding different values for the thermal expansion of interatomic distances and the linear thermal expansion coefficient, as discussed by Fornasini and co-workers.[31,32,62,84] For bulk *c*-Ge at 300 K, for example, our results from Ref. 36 yield $\alpha_{\mathrm{EXAFS}} = 11.0(\pm 1.0) \times 10^{-6}$ K^{-1}, in very good agreement with the EXAFS results of Ref. 31 but almost twice the value of $\alpha_L = 5.9 \times 10^{-6}$ K^{-1} determined from interferometric, calorimetric, and x-ray-diffraction measurements.[81]

TABLE II. Static contributions to the total disorder ($\sigma^2_{\mathrm{static}}$), Einstein temperatures (Θ_E), thermal expansion of interatomic bonds (ΔR), and linear coefficients of thermal expansion (α_{EXAFS}) between highest (300 K) and lowest (17 K) temperatures and anharmonic force constant (k_3) obtained for the Ge NCs and bulk *a*-Ge experimental data. Data for bulk *c*-Ge from Ref. 36 are also listed for comparison.

System	$\sigma^2_{\mathrm{static}}$ (10^{-3} Å^2)	Θ_E (K)	ΔR (10^{-3} Å)	α_{EXAFS} (10^{-6} K^{-1})	k_3 (eV/Å^3)
Bulk *a*-Ge	2.1 ± 0.1	343 ± 4	5.5 ± 1.2	8.0 ± 1.0	-10.5 ± 2.5
4 nm Ge NCs	2.0 ± 0.1	367 ± 5	2.1 ± 1.2	3.0 ± 1.0	-4.9 ± 1.5
5 nm Ge NCs	1.8 ± 0.1	360 ± 5	3.4 ± 1.2	5.0 ± 1.0	-5.6 ± 1.7
6 nm Ge NCs	1.3 ± 0.1	357 ± 5	3.7 ± 1.2	5.3 ± 1.0	-6.2 ± 1.8
9 nm Ge NCs	1.1 ± 0.1	352 ± 4	4.6 ± 1.2	6.7 ± 1.0	-6.9 ± 2.1
Bulk *c*-Ge [a]	0.1 ± 0.1	351 ± 7	7.2 ± 1.2	11.0 ± 1.0	-4.1 ± 1.2

[a]Reference 36.

We also stress that the values obtained from Eq. (2) depend only on the variation of the experimental interatomic distances and are not calculated from the anharmonicity of the pair potential, as first postulated in Ref. 34. Thus, they are related to the "real" distribution of distances as defined in Refs. 31 and 32 and are also sensitive to the effect of vibrations perpendicular to the bond direction.[31,32]

From Fig. 13 and Table II, the NCs exhibit significantly reduced thermal expansion of interatomic distances relative to the bulk phases in the measured interval, while *a*-Ge shows a slightly reduced thermal expansion relative to that of *c*-Ge. A clear trend with NC size is apparent, as for the Debye-Waller factor, and will be further discussed below.

The linear thermal expansion coefficient of silica is negative below ~180 K,[85–87] yet positive (though very low) above this temperature,[87,88] with a value of $\alpha_L = 0.4 \times 10^{-6}$ K^{-1} at 300 K.[89] Despite slight variation depending on the thermal history,[87,90] this value is always significantly smaller (about 1 order of magnitude) than that for bulk *c*-Ge at 300 K ($\alpha_L = 5.9 \times 10^{-6}$ K^{-1} from experimental and theoretical studies[81]). The thermal expansion of the NCs is thus likely to be hindered by the much lower expansion of the matrix. Furthermore, the presence of the thin amorphous Ge layer between the matrix and NC core may also contribute to the reduced thermal expansion.

We again comment on the possible influence of isotopic effects. EXAFS measurements yield differences of 2.1×10^{-4} and 0.5×10^{-4} Å for the first NN interatomic distances of bulk ^{70}Ge and ^{76}Ge at 20 and 300 K, respectively (the smaller interatomic distances for the heavier isotope).[80] The differences will be smaller between ^{Nat}Ge and ^{74}Ge and thus are not significant compared to the differences measured between the bulk and NCs in our study ($\geq 1.0 \times 10^{-3}$ Å), confirming that they stem from the properties of the nanocrystalline phase and the presence of a surrounding matrix. Note also that the NCs are composed on average of a heavier isotope, yet exhibit greater interatomic distances than those in bulk *c*-Ge.

3. Third cumulants and anharmonicity of the effective pair potential

The experimental values obtained for the EXAFS C_3, which accounts for asymmetric deviations from a Gaussian-type bond-length distribution, are shown in Fig. 14. Again we display values relative to that obtained for bulk *c*-Ge at low temperature for easier comparison. As detailed in Ref. 36, during the multiple-data set fits for all temperatures of a given sample we restrain the C_3 values to follow the relation derived from the anharmonic one-dimensional effective potential V_{eff} in Ref. 34:

$$C_3(T) = \frac{k_3 k_B^2 \Theta_E}{2k_{\text{eff}}^3} \frac{1 + 10z + z^2}{(1-z)^2} + C_{3\text{static}}. \quad (3)$$

Here $C_{3\text{static}}$ is the asymmetry from structural contributions, $z \equiv \exp(-\Theta_E/T)$, and $k_{\text{eff}} = \mu k_B^2 \hbar^{-2} \Theta_E^2$, where k_{eff} and k_3 are the effective harmonic spring constant and the cubic anharmonic force constant, respectively, entering the effective potential V_{eff} as follows:

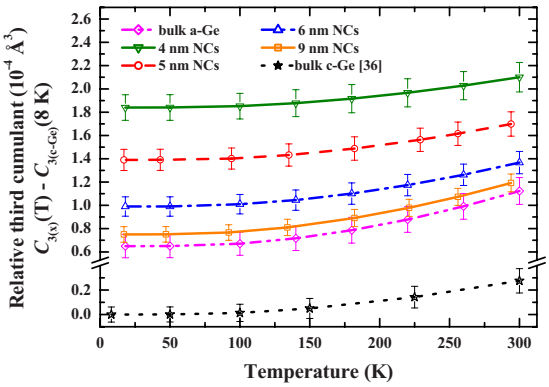

FIG. 14. (Color online) Third cumulant values obtained for the Ge NC and bulk *a*-Ge samples plotted as a function of measurement temperature (line with symbols). Values relative to the low-temperature value obtained for bulk *c*-Ge are shown to make comparison easier. Data for *c*-Ge from Ref. 36 are also plotted for comparison. Notice the break on the vertical axis between 0.40 and 0.53×10^{-4} Å^3.

$$V_{\text{eff}}(r - r_0) = k_{\text{eff}}(r - r_0)^2 + k_3(r - r_0)^3. \quad (4)$$

Such a restraint is well justified by results from previous works,[32,62] where unrestrained C_3 values were found to follow the form of Eq. (3). Furthermore it is needed to relate C_3 and Θ_E, which can be determined with better precision, as well as to reduce the correlations between R (which is floated, not restrained) and C_3. The thermal evolution of C_3, as described by the k_3 values, is listed in Table II.

We observe an increase in asymmetry with temperature in the measured range for all samples, as expected from the increase in anharmonicity of the effective potential. The increase in the thermal contribution to C_3 due to the anharmonicity of the effective potential is highest for *a*-Ge and, although higher for NCs than for *c*-Ge, shows a decrease with NC size. This size trend is further discussed in Sec. III C 4.

4. Size-dependent trends

Gathered in Fig. 15 are the size-dependent trends, for the first NN Ge shell, of: (a) the structural contribution to total disorder, (b) the thermal contribution to total disorder, (c) the thermal expansion of interatomic distances between 15 and 300 K, and (d) the anharmonic force constant for the effective potential. All parameters are well described by a linear evolution with the inverse NC diameter, confirming that thermal and vibrational properties are dominated by the structural properties of Ge NCs in the size range under evaluation.

As their size decreases, embedded Ge NCs exhibit an increase in mean interatomic distance, structural disorder, and asymmetry of the distribution of distances as a result of the combined effects of an increase in surface-to-volume ratio and the presence of a thin *a*-Ge-like layer between the *a*-SiO_2 matrix and Ge NC core. The decrease in NC size results in a higher fraction of atoms located on the NC surface. This invariably reduces the average coordination number, independent of the particles being crystalline or amorphous. But the increase in mean interatomic distance (approaching the values for bulk *a*-Ge) with the decrease in

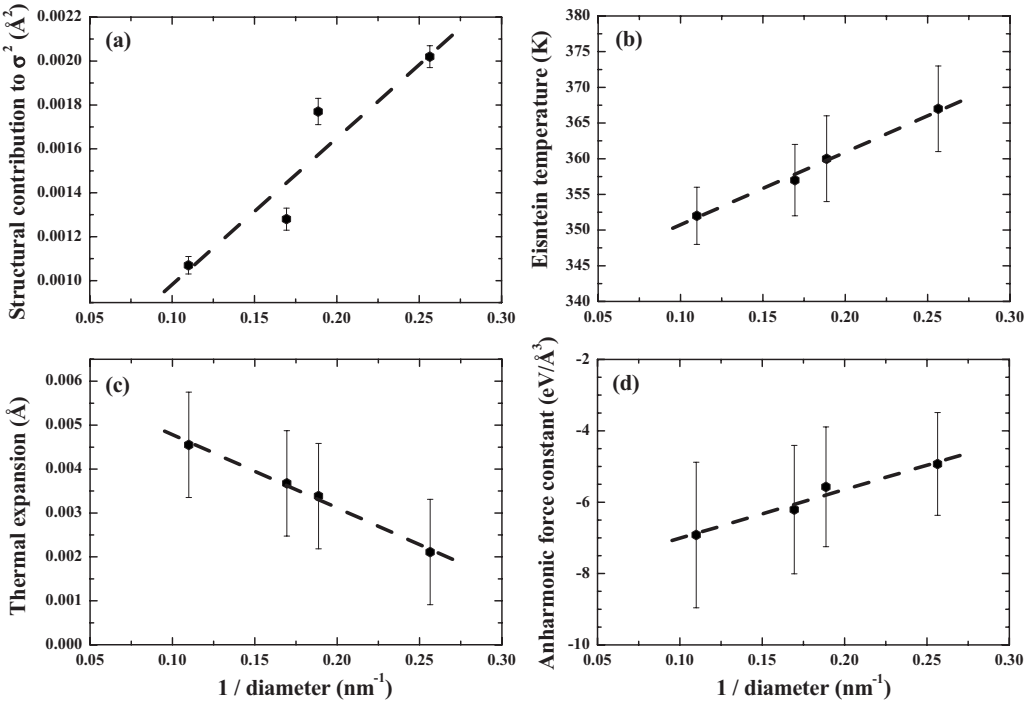

FIG. 15. Size-dependent trends obtained for the (a) static disorder, (b) thermal disorder and (c) thermal expansion between 15 and 300 K, and (d) anharmonic force constant of the 9, 6, 5, and 4 nm Ge NC distributions.

particle size demonstrates that the atoms which comprise the surface layer are in a disordered (and undercoordinated) state, the latter very similar to bulk *a*-Ge. This is further reinforced by the increase in structural disorder with decreasing size, which also approaches the value for bulk *a*-Ge. On the other hand, those atoms within the NC core maintain a bulklike crystalline structure, as apparent in TEM images and verified by XANES, EXAFS, and Raman measurements. If the atoms in the NC core were under compressive stress, we would expect a decrease in the mean interatomic distance, offsetting to some extent the increase due to disorder at the surface. Given that our results approach *a*-Ge-like values, we rule out a significant influence of stress from the matrix in our case. The coexistence of crystalline and amorphouslike environments with distinct interatomic distances also increases the asymmetry of the distance distribution such that C_3 is higher than for the bulk phases and increases as the size decreases. We anticipate that C_3 will decrease for smaller sizes as the amorphous fraction approaches 1. We note that the formation of a disordered surface layer surrounding a crystalline core was also observed for ~7.0 nm diameter freestanding Ge NCs produced by a gas-aggregation technique,[12] indicating that this phenomenon is intrinsic to the high surface-to-volume ratio (or very small particle size) and is not related to the presence of the silica matrix in our case. The variation in the Ge NC structural parameters with decreasing size described herein influences the thermal and vibrational properties, resulting in lower thermal expansion and higher Einstein temperature and anharmonicity of the effective pair potential. Part of the observed dampening of the thermal expansion is potentially the result of the silica matrix, which has a very low thermal expansion coefficient. But the matrix is not expected to significantly influence the mean vibrational frequency, since a similar increase has also been observed for other freestanding NCs,[91] where it was assigned mainly to surface reconstruction effects.

IV. CONCLUSIONS

Previously we observed that the atomic-scale structure of Ge NCs formed by ion implantation in a silica matrix exhibits increased disorder and asymmetry compared to bulk *c*-Ge.[5] Herein, we have shown that such perturbations are size dependent and increase with decreasing NC diameter. The linear variation of structural parameters with inverse diameter clearly demonstrates that the surface-to-volume ratio governs the structural properties of Ge NCs embedded in silica. Furthermore, we have presented evidence for the formation of an amorphous Ge layer separating the Ge crystalline core and the silica matrix. By combining SAXS and XANES results, we have observed that the concomitant decrease in NC size and increase in surface-to-volume ratio yields an amorphouslike Ge layer with constant thickness of ~0.44 nm. Our results suggest that very small Ge nanoparticles (<2.0 nm diameter) embedded in silica should be amorphous, in good agreement with molecular-dynamics results for Si nanoparticles of similar size embedded in the same matrix.[54] The formation of an amorphous interfacial layer was also observed experimentally for Si NCs embedded in silica in Ref. 55, where the impact of such a layer on the light-emission process was discussed. Light emission from Ge NCs embedded in silica may also be influenced by the presence of an amorphous layer between the crystalline core and amorphous matrix, since defects in this interfacial

layer may well serve as radiative and nonradiative recombination centers.

The temperature-dependent analysis confirmed that Ge NCs exhibit stiffer bonds/higher Einstein temperatures than those of bulk Ge (as previously observed in Ref. 36) and further revealed a linear increase in Einstein temperature with inverse NC diameter. Linear decreases in the thermal expansion of interatomic distances and in the anharmonic force constant were also observed as the inverse NC diameter increased. Such size trends confirm that the thermal and vibrational properties of the Ge NCs under study are mainly governed by the surface-to-volume ratio and the surface reconstruction through the formation of an amorphouslike Ge layer between the NC core and matrix, both yielding structural changes whose magnitude vary with NC size. There is also a further constricting effect of the rigid a-SiO_2 matrix, reducing the thermal expansion of the NCs. The results presented here should aid in explaining previously reported observations and contribute to the more efficient and rapid integration of Ge NCs in modern technologies.

ACKNOWLEDGMENTS

The authors thank the Australian Research Council and the Australian Synchrotron Research Program for financial support. L.L.A. and M.C.R. thank T. Mernagh of Geoscience Australia for access to the Raman spectrometer. L.L.A. acknowledges the Brazilian Research Agency CNPq for support. Portions of this research were performed at ChemMatCARS Sector 15 of the Advanced Photon Source, principally supported by the National Science Foundation/Department of Energy under Grant No. CHE0087817 and by the Illinois Board of Higher Education. The Advanced Photon Source is supported by the U.S. Department of Energy, Basic Energy Science, Office of Science, under Contract No. W-31-109-Eng-38.

*lla109@rsphysse.anu.edu.au

[1] S. K. Ray and K. Das, Opt. Mater. (Amsterdam, Neth.) **27**, 948 (2005).
[2] A. Singha, A. Roy, D. Kabiraj, and D. Kanjilal, Semicond. Sci. Technol. **21**, 1691 (2006).
[3] C. J. Park, K. H. Cho, W. C. Yang, H. Y. Cho, S. H. Choi, R. G. Elliman, J. H. Han, and C. Kim, Appl. Phys. Lett. **88**, 071916 (2006).
[4] H. W. Chiu, C. N. Chervin, and S. M. Kauzlarich, Chem. Mater. **17**, 4858 (2005).
[5] M. C. Ridgway, G. de M. Azevedo, R. G. Elliman, C. J. Glover, D. J. Llewellyn, R. Miller, W. Wesch, G. J. Foran, J. Hansen, and A. Nylandsted-Larsen, Phys. Rev. B **71**, 094107 (2005).
[6] C. Bostedt, T. v. Buuren, J. M. Plitzko, T. Möller, and L. J. Terminello, J. Phys.: Condens. Matter **15**, 1017 (2003).
[7] S. Sato, S. Nozaki, and H. Morisaki, Appl. Phys. Lett. **72**, 2460 (1998).
[8] T. P. L. Pedersen, J. S. Jensen, J. Chevallier, O. Hansen, J. M. Jensen, B. B. Nielsen, and A. N. Larsen, Appl. Phys. A: Mater. Sci. Process. **81**, 1591 (2005).
[9] C. Bonafos, B. Garrido, M. Lopez, A. Perez-Rodriguez, J. R. Morante, Y. Kihn, G. Ben Assayag, and A. Claverie, Mater. Sci. Eng., B **69-70**, 380 (2000).
[10] Y. Kanemitsu, H. Uto, Y. Masumoto, and Y. Maeda, Appl. Phys. Lett. **61**, 2187 (1992).
[11] A. V. Kolobov, S. Q. Wei, W. S. Yan, H. Oyanagi, Y. Maeda, and K. Tanaka, Phys. Rev. B **67**, 195314 (2003).
[12] C. Bostedt, T. van Buuren, T. M. Willey, N. Franco, T. Moller, and L. Terminello, J. Electron Spectrosc. Relat. Phenom. **126**, 117 (2002).
[13] J. M. J. Lopes, F. C. Zawislak, M. Behar, P. F. P. Fichtner, L. Rebohle, and W. Skorupa, J. Appl. Phys. **94**, 6059 (2003).
[14] M. Fujii, S. Hayashi, and K. Yamamoto, Jpn. J. Appl. Phys., Part 1 **30**, 687 (1991).
[15] I. D. Sharp, Q. Xu, C. Y. Liao, D. O. Yi, J. W. Beeman, Z. Liliental-Weber, K. M. Yu, D. N. Zakharov, J. W. Ager, D. C. Chrzan, and E. E. Haller, J. Appl. Phys. **97**, 124316 (2005).
[16] A. Wellner, V. Paillard, C. Bonafos, H. Coffin, A. Claverie, B. Schmidt, and K. H. Heinig, J. Appl. Phys. **94**, 5639 (2003).
[17] A. V. Kolobov, J. Appl. Phys. **87**, 2926 (2000).
[18] K. H. Heinig, B. Schmidt, A. Markwitz, R. Grotzschel, M. Strobel, and S. Oswald, Nucl. Instrum. Methods Phys. Res. B **148**, 969 (1999).
[19] J. S. Jensen, T. P. L. Pedersen, R. Pereira, J. Chevallier, J. L. Hansen, B. B. Nielsen, and A. N. Larsen, Appl. Phys. A: Mater. Sci. Process. **83**, 41 (2006).
[20] V. Cantelli, J. von Borany, A. Mucklich, and N. Schell, Nucl. Instrum. Methods Phys. Res. B **238**, 268 (2005).
[21] A. Markwitz, L. Rebohle, H. Hofmeister, and W. Skorupa, Nucl. Instrum. Methods Phys. Res. B **147**, 361 (1999).
[22] J. G. Zhu, C. W. White, J. D. Budai, S. P. Withrow, and Y. Chen, J. Appl. Phys. **78**, 4386 (1995).
[23] A. J. Williamson, C. Bostedt, T. Van Buuren, T. M. Willey, L. J. Terminello, G. Galli, and L. Pizzagalli, Nano Lett. **4**, 1041 (2004).
[24] H. Modrow, Appl. Spectrosc. Rev. **39**, 183 (2004).
[25] A. Meldrum, R. F. Haglund, L. A. Boatner, and C. W. White, Adv. Mater. (Weinheim, Ger.) **13**, 1431 (2001).
[26] G. E. J. Koops, H. Pattyn, A. Vantomme, S. Nauwelaerts, and R. Venegas, Phys. Rev. B **70**, 235410 (2004).
[27] Q. Xu, I. D. Sharp, C. W. Yuan, D. O. Yi, C. Y. Liao, A. M. Glaeser, A. M. Minor, J. W. Beeman, M. C. Ridgway, P. Kluth, J. W. Ager, D. C. Chrzan, and E. E. Haller, Phys. Rev. Lett. **97**, 155701 (2006).
[28] W. H. Li, S. Y. Wu, C. C. Yang, S. K. Lai, K. C. Lee, H. L. Huang, and H. D. Yang, Phys. Rev. Lett. **89**, 135504 (2002).
[29] E. Roduner, Chem. Soc. Rev. **35**, 583 (2006).
[30] L. Pizzagalli, G. Galli, J. E. Klepeis, and F. Gygi, Phys. Rev. B **63**, 165324 (2001).
[31] P. Fornasini, in *X-Ray Absorption Fine Structure–XAFS13: 13th International Conference*, edited by B. Hedman and P. Pianetta, AIP Conf. Proc. No. 882 (AIP, New York, 2007), p. 94.
[32] P. Fornasini, S. a Beccara, G. Dalba, R. Grisenti, A. Sanson, M. Vaccari, and F. Rocca, Phys. Rev. B **70**, 174301 (2004).

[33] L. Troger, T. Yokoyama, D. Arvanitis, T. Lederer, M. Tischer, and K. Baberschke, Phys. Rev. B **49**, 888 (1994).
[34] A. I. Frenkel and J. J. Rehr, Phys. Rev. B **48**, 585 (1993).
[35] P. Kluth, B. Johannessen, L. L. Araujo, and M. C. Ridgway, in *X-Ray Absorption Fine Structure–XAFS13: 13th International Conference*, edited by B. Hedman and P. Pianetta, AIP Conf. Proc. No. 882 (AIP, New York, 2007), p. 731.
[36] L. L. Araujo, P. Kluth, G. de M. Azevedo, and M. C. Ridgway, Phys. Rev. B **74**, 184102 (2006).
[37] L. R. Doolittle, Nucl. Instrum. Methods Phys. Res. B **9**, 344 (1985).
[38] J. Ilavsky, available at http://usaxs.xor.aps.anl.gov/staff/ilavsky/irena.html
[39] J. A. Potton, G. J. Daniell, and B. D. Rainford, J. Appl. Crystallogr. **21**, 663 (1988).
[40] J. A. Potton, G. J. Daniell, and B. D. Rainford, J. Appl. Crystallogr. **21**, 891 (1988).
[41] A. Cheung, G. D. Azevedo, C. J. Glover, D. J. Llewellyn, R. G. Elliman, G. J. Foran, and M. C. Ridgway, Appl. Phys. Lett. **84**, 278 (2004).
[42] J. Hester, available at http://anbf2.kek.jp/xafs-downloads.html
[43] B. Ravel and M. Newville, J. Synchrotron Radiat. **12**, 537 (2005).
[44] M. Newville, J. Synchrotron Radiat. **8**, 322 (2001).
[45] J. J. Rehr and R. C. Albers, Rev. Mod. Phys. **72**, 621 (2000).
[46] S. D. Kelly and B. Ravel, in *X-Ray Absorption Fine Structure–XAFS13: 13th International Conference*, edited by B. Hedman and P. Pianetta, AIP Conf. Proc. No. 882 (AIP, New York, 2007), p. 132.
[47] L. L. Araujo, G. J. Foran, and M. C. Ridgway, J. Phys.: Condens. Matter **20**, 165210 (2008).
[48] D. Haskel, B. Ravel, M. Newville, and E. A. Stern, Physica B (Amsterdam) **208-209**, 151 (1995).
[49] W. K. Chu, J. W. Mayer, and M. A. Nicolet, *Backscattering Spectrometry* (Academic, New York, 1978).
[50] A. R. Wilkinson and R. G. Elliman, Appl. Phys. Lett. **83**, 5512 (2003).
[51] A. Bianconi, Appl. Surf. Sci. **6**, 392 (1980).
[52] A. Bianconi, A. Di Cicco, N. V. Pavel, M. Benfatto, A. Marcelli, C. R. Natoli, P. Pianetta, and J. Woicik, Phys. Rev. B **36**, 6426 (1987).
[53] L. Pizzagalli and G. Galli, Mater. Sci. Eng., B **96**, 86 (2002).
[54] F. Djurabekova and K. Nordlund, Phys. Rev. B **77**, 115325 (2008).
[55] N. Daldosso, M. Luppi, S. Ossicini, E. Degoli, R. Magri, G. Dalba, P. Fornasini, R. Grisenti, F. Rocca, L. Pavesi, S. Boninelli, F. Priolo, C. Spinella, and F. Iacona, Phys. Rev. B **68**, 085327 (2003).
[56] M. C. Ridgway, G. D. Azevedo, C. J. Glover, R. G. Elliman, D. J. Llewellyn, A. Cheung, B. Johannessen, D. A. Brett, and G. J. Foran, Nucl. Instrum. Methods Phys. Res. B **218**, 421 (2004).
[57] A. I. Frenkel, A. V. Kolobov, I. K. Robinson, J. O. Cross, Y. Maeda, and C. E. Bouldin, Phys. Rev. Lett. **89**, 285503 (2002).
[58] J. Gonzalez-Hernandez, G. H. Azarbayejani, R. Tsu, and F. H. Pollak, Appl. Phys. Lett. **47**, 1350 (1985).
[59] H. Richter, Z. P. Wang, and L. Ley, Solid State Commun. **39**, 625 (1981).
[60] M. Cardona and M. L. W. Thewalt, Rev. Mod. Phys. **77**, 1173 (2005).
[61] G. Bunker, Nucl. Instrum. Methods Phys. Res. **207**, 437 (1983).
[62] G. Dalba, P. Fornasini, R. Grisenti, and J. Purans, Phys. Rev. Lett. **82**, 4240 (1999).
[63] P. Eisenberger and G. S. Brown, Solid State Commun. **29**, 481 (1979).
[64] G. Dalba, P. Fornasini, R. Grisenti, and F. Rocca, J. Non-Cryst. Solids **345-346**, 7 (2004).
[65] A. Filipponi and A. Di Cicco, Phys. Rev. B **51**, 12322 (1995).
[66] P. Kluth, B. Johannessen, V. Giraud, A. Cheung, C. J. Glover, G. D. Azevedo, G. J. Foran, and M. C. Ridgway, Appl. Phys. Lett. **85**, 3561 (2004).
[67] B. S. Clausen and J. K. Norskov, Top. Catal. **10**, 221 (2000).
[68] G. Kresse and J. Hafner, Phys. Rev. B **49**, 14251 (1994).
[69] M. C. Ridgway, C. J. Glover, K. M. Yu, G. J. Foran, C. Clerc, J. L. Hansen, and A. Nylandsted Larsen, Phys. Rev. B **61**, 12586 (2000).
[70] T. Kawamura, O. Shimomura, T. Fukamachi, and P. H. Fuoss, Acta Crystallogr., Sect. A: Cryst. Phys., Diffr., Theor. Gen. Crystallogr. **37**, 653 (1981).
[71] A. I. Frenkel, C. W. Hills, and R. G. Nuzzo, J. Phys. Chem. B **105**, 12689 (2001).
[72] W. H. Qi, M. P. Wang, and Y. C. Su, J. Mater. Sci. Lett. **21**, 877 (2002).
[73] B. Johannessen, P. Kluth, D. J. Llewellyn, G. J. Foran, D. J. Cookson, and M. C. Ridgway, Appl. Phys. Lett. **90**, 073119 (2007).
[74] B. Johannessen, P. Kluth, D. J. Llewellyn, G. J. Foran, D. J. Cookson, and M. C. Ridgway, Phys. Rev. B **76**, 184203 (2007).
[75] C. J. Glover, M. C. Ridgway, D. J. Llewellyn, P. Kluth, and B. Johannessen, Nucl. Instrum. Methods Phys. Res. B **238**, 306 (2005).
[76] J. K. Bording, Phys. Rev. B **62**, 7103 (2000).
[77] L. L. Araujo, R. Giulian, B. Johanessen, D. J. Llewellyn, P. Kluth, G. D. Azevedo, D. J. Cookson, and M. C. Ridgway, Nucl. Instrum. Methods Phys. Res. B **266**, 3153 (2008).
[78] G. Dalba, P. Fornasini, R. Grisenti, F. Rocca, I. Chambouleyron, and C. F. O. Graeff, J. Phys.: Condens. Matter **9**, 5875 (1997).
[79] E. D. Crozier and A. J. Seary, Can. J. Phys. **59**, 876 (1981).
[80] J. Purans, N. D. Afify, G. Dalba, R. Grisenti, S. De Panfilis, A. Kuzmin, V. I. Ozhogin, F. Rocca, A. Sanson, S. I. Tiutiunnikov, and P. Fornasini, Phys. Rev. Lett. **100**, 055901 (2008).
[81] Y. Ma and J. S. Tse, Solid State Commun. **143**, 161 (2007).
[82] A. Kazimirov, J. Zegenhagen, and M. Cardona, Science **282**, 930 (1998).
[83] M. Y. Hu, H. Sinn, A. Alatas, W. Sturhahn, E. E. Alp, H. C. Wille, Y. V. Shvyd'ko, J. P. Sutter, J. Bandaru, E. E. Haller, V. I. Ozhogin, S. Rodriguez, R. Colella, E. Kartheuser, and M. A. Villeret, Phys. Rev. B **67**, 113306 (2003).
[84] G. Dalba and P. Fornasini, J. Synchrotron Radiat. **4**, 243 (1997).
[85] H. T. Smyth, J. Am. Ceram. Soc. **38**, 140 (1955).
[86] D. F. Gibbons, J. Phys. Chem. Solids **11**, 246 (1959).
[87] G. K. White, J. Phys. D **6**, 2070 (1973).
[88] P. H. Gaskell, Trans. Faraday Soc. **62**, 1505 (1966).
[89] J. M. Shackelford and W. Alexander, *CRC Materials Science and Engineering Handbook* (CRC, Boca Raton, FL, 2001).
[90] W. A. Plummer and H. E. Hagy, Appl. Opt. **7**, 825 (1968).
[91] Q. F. Gu, G. Krauss, F. Gramm, A. Cervellino, and W. Steurer, Phys. Rev. Lett. **100**, 045502 (2008).